Journal of Biomedical Optics

SPIEDigitalLibrary.org/jbo

In vitro and *in vivo* three-dimensional velocity vector measurement by three-beam spectral-domain Doppler optical coherence tomography

Wolfgang Trasischker
René M. Werkmeister
Stefan Zotter
Bernhard Baumann
Teresa Torzicky
Michael Pircher
Christoph K. Hitzenberger

SPIE

In vitro and *in vivo* three-dimensional velocity vector measurement by three-beam spectral-domain Doppler optical coherence tomography

Wolfgang Trasischker, René M. Werkmeister, Stefan Zotter, Bernhard Baumann, Teresa Torzicky, Michael Pircher, and Christoph K. Hitzenberger
Medical University of Vienna, Center for Medical Physics and Biomedical Engineering, Waehringer Guertel 18-20, A-1090 Vienna, Austria

Abstract. We developed a three-beam Doppler optical coherence tomography (OCT) system that enables measurement of the velocity vector of moving particles in three-dimensions (3-D). The spatial orientation as well as the magnitude of motion can be determined without prior knowledge of the geometry of motion. The system combines three spectral-domain OCT interferometers whose sample beams are focused at the sample by a common focusing lens at three different angles. This provides three spatially independent velocity components simultaneously from which the velocity vector can be reconstructed. We demonstrate the system in a simple test object (rotating disc), a flow phantom, and for blood flow measurements in the retina of a healthy human subject. Measurements of blood flow at a venous bifurcation achieve a good agreement between in- and outflow and demonstrate the reliability of the method. [DOI: 10.1117/1.JBO.18.11.116010]

Keywords: optical coherence tomography; Doppler; flow measurement; multibeam; retina.

Paper 130354RR received May 16, 2013; revised manuscript received Sep. 30, 2013; accepted for publication Oct. 21, 2013; published online Nov. 18, 2013.

1 Introduction

Optical coherence tomography (OCT) was introduced more than two decades ago[1] as a noninvasive modality for imaging transparent and translucent tissues with a resolution of a few micrometers.[2,3] The first (and still dominating) application field of OCT was ophthalmology, where OCT revolutionized retinal imaging and diagnostics.[4,5] In the later years, several functional extensions of OCT were developed, one of the most promising being Doppler OCT (DOCT)[6–8] which provides information on the movement of backscattering particles. Since major eye diseases such as diabetic retinopathy and glaucoma, as well as disorders such as retinal branch vein occlusion, are associated with alterations in blood perfusion, DOCT is of special interest for ophthalmic imaging.

A variety of different DOCT techniques have been reported in the literature. Examples are time domain-based optical Doppler tomography,[9] phase-resolved DOCT (PR-DOCT),[10–13] resonant Doppler flow imaging,[14] joint spectral and time domain imaging,[15,16] optical micro-angiography[17,18] or single-pass volumetric bidirectional blood flow imaging.[19]

Apart from phase-based techniques, further principles can be used to obtain velocity information from OCT data. By using time varying speckle,[20] it was possible to provide quantitative flow information for measurements on a flow phantom and *in vivo*. Although being able to detect motions normal to the optical axis, this technique cannot determine the direction of flow. Autocorrelation techniques[21,22] utilize the statistical nature of intensity fluctuations of light backscattered by flowing particles. This technique was experimentally verified by using a flow phantom. Integrating dynamic light scattering and OCT (Ref. 23) is capable of distinguishing diffuse from translational motions and can measure axial and transverse components of the flow velocity. However, long measurement times are necessary and so far the computational effort for this technique is very high compared to conventional DOCT techniques.

In this work, we strive to obtain absolute quantitative and directional information on the flow, for which methods based on phase measurements are well suited. With these methods, the phase difference, $\Delta\Phi$, between signals of adjacent A-scans at partially overlapping positions is measured. The obtained $\Delta\Phi$ is directly proportional to the axial velocity component, V_{axial}, at the measured sample position

$$V_{\text{axial}} = \vec{e} \cdot \vec{V} = \frac{\lambda \Delta\Phi}{4\pi\tau n}, \tag{1}$$

where $\vec{e}$ is the unit vector in beam direction, $\vec{V}$ is the velocity vector, λ is the central wavelength of the illuminating light, τ is the time period between successive A-scans, and n denotes the refractive index of the medium that contains the scattering particle. Equation (1) illustrates a limitation of common PR-DOCT: only the velocity component parallel to the direction of observation, V_{axial}, can be measured. This is indicated by the scalar product of the vectors $\vec{e}$ and $\vec{V}$. If the angle α between these two vectors is equal to 90 deg, the phase shift is zero and no velocity can be measured. Knowing α can help to overcome the geometrical limitation and provides the absolute velocity

$$|\vec{V}| = \left| \frac{V_{\text{axial}}}{\cos(\alpha)} \right|. \tag{2}$$

The Doppler angle α can be obtained from the structural data extracted from multiple 2-D or 3-D OCT data sets.[24,25]

Address all correspondence to: Christoph K. Hitzenberger, Center for Medical Physics and Biomedical Engineering, Waehringer Guertel 18-20, A-1090 Vienna, Austria. Tel: +431-40400-39224; Fax: +431-40400-3988; E-mail: christoph.hitzenberger@meduniwien.ac.at

From the 3-D image geometry, the vessel orientation, and hence the angle α, can be determined. However, if the measurements are performed in living tissue, motion artifacts during data acquisition frequently distort the 3-D geometry of the image, and the vessel orientation (and hence α) is unreliable.

Another option to overcome this problem is the use of two or more sampling beams simultaneously. Different variants of two- and multibeam setups have been reported for DOCT. Approaches that use two beams scanning the retina in parallel with a time delay were successfully demonstrated to extend the range of accessible velocities down to very low velocity values, thereby enabling improved contrast for small retinal vessels and capillaries.[26–28] A combination of this approach with a statistical method based on temporal cross correlation was recently shown to provide quantitative and directional velocity information in flow phantoms.[29]

To solve the problem of the unknown Doppler angle directly, beams that sample the moving scatterers simultaneously from different directions can be used.[30–34] Thereby, the individual components of the Doppler vector can be measured simultaneously and the angular dependence is avoided.

By using two orthogonally polarized beams produced by a Wollaston prism, the first dual beam DOCT setup with bidirectional probing was realized.[30] Successful measurements were demonstrated for the flow profile in glass capillaries. Using a trigonometric approximation in order to account for the orientation between illuminating beams and capillaries, the system was independent of the angle of incidence for angles close to 90 deg. One drawback of this approach was that only two beams were used, providing just two components of the velocity vector, therefore, additional information on the capillary orientation was necessary to obtain the absolute velocity. This technique was further improved and *in-vivo* applications in the human eye were reported.[34,35] Although still limited to measure only two components of the velocity vector directly, the third dimension could be retrieved by measuring the azimuth angle of the retinal vessel from a fundus image. Recently, this technique was extended by rotating the orientation of the plane spanned by the dual-beam geometry with a mechanically driven Dove prism.[36] Proper alignment of the beam geometry with respect to the imaged blood vessels can provide the absolute velocity vector from just two sampling beams. However, the proper alignment of the Dove prism complicates the measurement since it requires a priori knowledge of the investigated vessel geometry.

PR-DOCT systems acquiring all the three velocity vector components, without using additional structural data for the velocity reconstruction, have been reported on a very limited basis in the literature.[31,33]

A very compact design used a single beam and divided its cross section into three segments with a beam divider consisting of a glass plate with sectors of different thickness. After directing the different cross-sectional segments of the beam through a focusing lens, different measurement orientations were achieved. The velocity information corresponding to the three components is encoded in depth due to the different optical path lengths of the components within the three-segment beam divider. This approach showed promising results for *in-vitro* applications.[33] An advantage of this method is that the three velocity components along one depth profile can be recorded with a single A-scan. This, however, severely limits the achievable depth range.

The purpose of this work is to present a new improved PR-DOCT system that overcomes the limitations mentioned above. The instrument uses three separate sampling beams which provide access to the three components of the velocity vector. This enables the reconstruction of the absolute velocity vector without requiring any additional information on vessel orientation from structural data, thus avoiding any artifacts due to the sample motion. Furthermore, the use of three independent channels in parallel effectively eliminates any cross talk[37] and provides full ranging depth for each channel. We demonstrate the performance of the system by calibration measurements in a rotating disk, by measurements in a capillary flow phantom of well-defined flow, and by analyzing the flow in a venous bifurcation in the retina of a healthy volunteer.

2 Methods

2.1 *Experimental Setup*

2.1.1 *Sampling beam geometry*

Our three-beam DOCT system employs a special sampling beam geometry depicted in Fig. 1. Three parallel sampling beams, separated from each other by equal distances, illuminate a joint focusing lens which focuses them to a mutual spot on the sample. This yields the geometry of an equilateral triangle-based pyramid, with the tip of the pyramid being the mutual focal spot of the respective beams (see Fig. 1). Knowledge of the distance between the parallel beams and the focal length of the lens provides all information necessary to determine the exact spatial orientation of the three measurement beams. Reconsidering Eq. (1) and expressing it for each measuring direction yields a system of three equations with three unknown coefficients:

$$\begin{array}{l} V_{\text{axial-1}} = \vec{e}_1 \cdot \vec{V} \\ V_{\text{axial-2}} = \vec{e}_2 \cdot \vec{V} \\ V_{\text{axial-3}} = \vec{e}_3 \cdot \vec{V} \end{array} \rightarrow \begin{array}{l} V_{\text{axial-1}} = e_{1-x} \cdot V_x + e_{1-y} \cdot V_y + e_{1-z} \cdot V_z \\ V_{\text{axial-2}} = e_{2-x} \cdot V_x + e_{2-y} \cdot V_y + e_{2-z} \cdot V_z \\ V_{\text{axial-3}} = e_{3-x} \cdot V_x + e_{3-y} \cdot V_y + e_{3-z} \cdot V_z \end{array}. \tag{3}$$

The unknown coefficients in Eq. (3) are the three components of the velocity vector, V_x, V_y, V_z, and can be determined by solving the system of equations.

2.1.2 *Interferometer setup*

Our system is based on spectral domain (SD)-OCT (Refs. 38–40). A schematic drawing of the three-beam DOCT system is shown in Fig. 2 and a description can be found in the following. The experimental setup combines three SD-OCT systems. We employ three similar superluminescent diodes (SLD) (EXS0840, Exalos, Switzerland) emitting light centered at a wavelength around 840 nm with a bandwidth of 50 nm. The SLDs are coupled to single mode fibers, guiding the light to a set of miniature collimators (beam diameter ~500 μm). An in-house designed mount, machined out of one piece of brass, aligns the laser beams according to the corners of an equilateral triangle. This mono-block construction avoids temperature and vibration drifts between the beams. The beams are aligned parallel to each other with a beam distance of 4.4 mm. The three beams are directed toward a nonpolarizing bulk beam splitter which separates the respective beams into the sample and reference arms. For *in-vitro* measurements, we use a

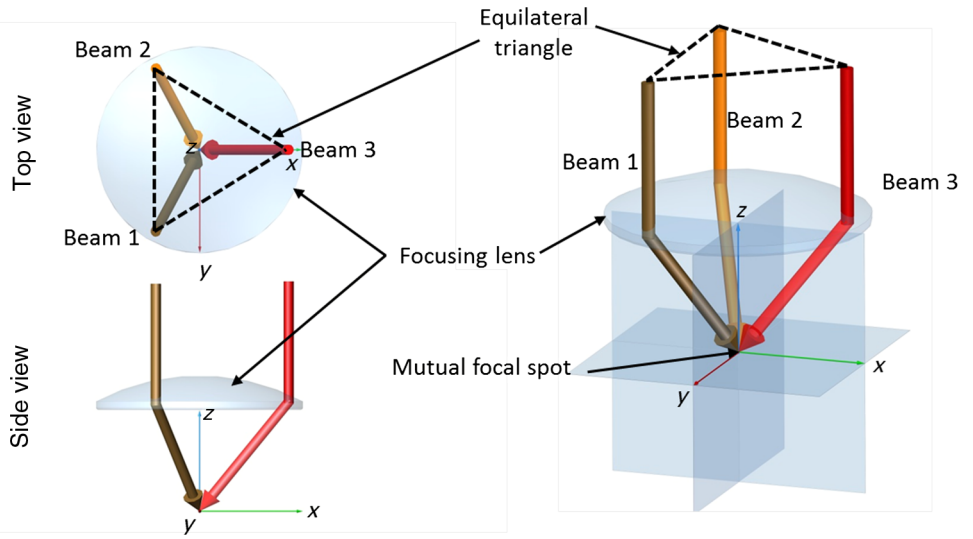

Fig. 1 Schematic diagram of the three beams measurement geometry: top- and side-view on the left, three-dimensional (3-D) model on the right.

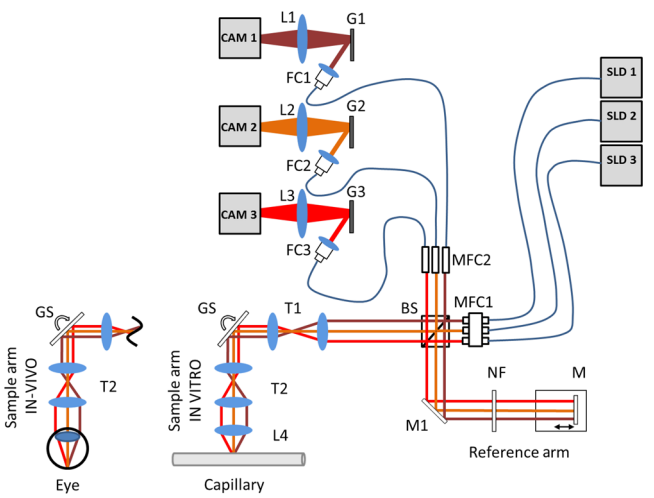

Fig. 2 Sketch of the experimental setup: SLD_{1-3}, superluminescent diode; BS, nonpolarizing beam splitter; $M_{1,r}$, mirror; NF, neutral density filter; T_{1-2}, telescope; GS, galvo scanner; L_{1-4}, lens; FC_{1-3}, fiber collimator; MFC_{1-2}, miniature fiber collimator; G_{1-3}, reflection grating (1200 lines/mm); CAM_{1-3}, line-scan camera. For the sample arm the two possible layouts, *in vitro* and *in vivo*, are depicted next to each other at the bottom left.

50/50 (R/T) splitter, while for *in-vivo* applications in the eye, we use a 70/30 (R/T) splitting ratio.

In the sample arm, two telescopes are used in order to set the beam distance. The first telescope, T_1, has a focal length ratio of 100/30 and is used to achieve a narrow beam spacing at the galvo scanner. Having three beams located at the corners of a triangle, it is impossible to provide all beams to be at the pivot axis of the scanner. An off-axis position introduces phase shifts due to the scanner movement.[41] Decreasing the beam distance simultaneously reduces the phase shift and minimizes fringe washout. Remaining phase shifts can then be compensated for in postprocessing.

With the second telescope, T_2, featuring a focal length ratio of 30/80, the beam distance is increased to a value satisfying the needs for *in-vitro* and *in-vivo* measurements. A distance of 3.5 mm provides a substantially different inclination of the measurement beams with respect to each other and simultaneously allows for the penetration of a dilated human pupil with all three measurement beams.

For the *in-vitro* case, an objective lens focuses the beams to a mutual spot on the sample while for *in-vivo* measurements this is performed by the refractive optics of the human eye. It is important that the optical axis of the final lens and the equilateral triangular-based pyramid height coincide to produce the measurement geometry described above. The distance between the parallel beams after the second telescope, T_2, and the focal length of the final lens, or the eye length, determines the actual orientation of each measurement direction. In order to ensure the correct measurement geometry for *in-vitro* measurements, the beam distance was checked by a charge coupled device (CCD) camera at several positions before and after the mutual focusing lens. The obtained actual geometry was in very good agreement with the expected values.

In the reference arm all three beams pass a neutral density filter, which is used to set the light power at the detection unit close to the saturation level of the CCD line-scan cameras.

Finally, backscattered light from the sample is recombined with the light reflected at the reference mirror at the beam splitter and coupled to a second set of miniature collimators. Single mode fibers guide the light toward three identical spectrometer units, consisting of a collimator, blazed reflective grating (1200 lines/mm), focusing lens ($f = 200$ mm), and a line-scan camera (Atmel Aviiva, 2048 pixels). During all our measurements, the cameras are operated at a line-scan frequency of 20 kHz.

The system combines three individual SD-OCT setups and requires an accordingly higher effort in terms of setup building and alignment. Especially, a careful alignment of the spectrometer units to provide similar phase characteristics with depth of the Fourier transformed signals in all three channels is necessary. The final bulk size of the entire setup fitted on an average sized optical table (75×100 cm) as can be seen in Fig. 3. However, while the system is presently rather bulky, the complexity may be reduced in future versions of the instrument by replacing the three separate detection units by a single camera system with joint spectrometer optics.[42–44]

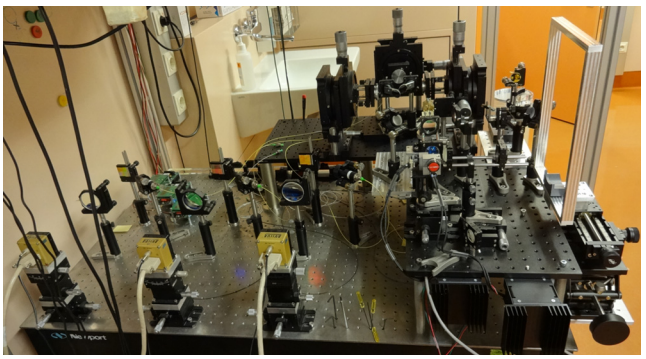

Fig. 3 Picture of the entire setup as used for *in vivo* eye measurements.

For the *in-vitro* measurements an illumination power of 700 μW per beam is set, adding to a total illumination power of 2.1 mW and leading to a measured sensitivity (close to zero delay) of 98 dB per channel. However, for *in-vivo* measurements, the illumination power is decreased to 700 μW in total or 233 μW per beam, which is below the lasers safety limits.[45,46] With the lower illumination power, a sensitivity of 95 dB was measured for each channel.

2.2 *Signal Processing*

All three beams measure the same spot at the sample simultaneously. During postprocessing, the three measurement directions can be regarded as independent and each channel is first evaluated individually in terms of intensity and Doppler data. Then, the velocity data along the different measurement directions is combined to compute the absolute velocity vector according to Eq. (3).

In a first step, intensity images are generated by standard SD-OCT preprocessing procedures (mean spectrum subtraction, rescaling from wavelength to wavenumber space, zero padding, dispersion correction, and inverse Fourier transform). In a second step, the phase difference of adjacent A-scans is calculated. In order to eliminate background phase noise, we compute this phase difference only for pixels above a certain intensity threshold level (typically four times the intensity noise level). This leaves us with three independent phase difference tomograms of the same position in the sample. Due to the mono-block construction of the miniature collimator mount and the bulk optics interferometer setup, our system is very phase stable. No phase drift correction is needed along one B-scan. However, it is necessary to correct for the phase shift introduced by the galvo scanner. To do so, we apply a histogram-based method[13] for each channel. Under the assumption that more static than dynamic tissue is imaged, we compute a phase histogram of an entire B-scan. This histogram reveals the phase shift introduced by the scanner and bulk motion (e.g., head movement during the measurement). Subtracting the most populated histogram value from all the other pixel values in the B-scan results in a phase shift corrected image.

To improve the signal quality, several B-scans are averaged (for each channel separately) by an algorithm working in complex space.[47] Before the averaging, B-scans have to be aligned to eliminate bulk motion artifacts. For *in-vitro* measurements, no sample bulk motion is present, making a motion correction unnecessary. The averaging is typically applied over 20 B-scans. For *in-vivo* evaluation, a basic eye motion correction is performed, which correlates the position of vessel centers within the different B-scans to each other. Using the number of B-scans that are recorded during the time of one heartbeat, we average over the systolic and diastolic phase of one pulse. This typically led to 15 averaged B-scans for the *in-vivo* measurement.

Extending Eq. (1) to a two-dimensional (2-D) set of phase information recorded for three different measurement directions and including the phase shift correction, $\Phi_{\text{shift-}k}$, leads to Eq. (4)

$$V_{\text{axial-}k-ij} = \vec{e}_k \cdot \vec{V}_{ij} = \frac{\lambda(\Delta\Phi_{k-ij} - \Phi_{\text{shift-}k})}{4\pi\tau n}. \quad (4)$$

The index k runs from 1 to 3 and indicates the individual measurement directions while the indices i and j indicate the position of the respective pixel in the B-scan. According to Eq. (4), the averaged phase images are rescaled to the velocity measured along the respective beam direction for every pixel in one B-scan. This yields the axially measured velocity components $V_{\text{axial-1}-ij}$, $V_{\text{axial-2}-ij}$, $V_{\text{axial-3}-ij}$.

Applying Eq. (3) to the case of 2-D data sets yields Eq. (5)

$$\begin{aligned} V_{\text{axial-1}-ij} &= \frac{\lambda(\Delta\Phi_{1-ij} - \Phi_{\text{shift}-1})}{4\pi\tau n} \\ &= e_{1-x} \cdot V_{x-ij} + e_{1-y} \cdot V_{y-ij} + e_{1-z} \cdot V_{z-ij} \\ V_{\text{axial-2}-ij} &= \frac{\lambda(\Delta\Phi_{2-ij} - \Phi_{\text{shift}-2})}{4\pi\tau n} \\ &= e_{2-x} \cdot V_{x-ij} + e_{2-y} \cdot V_{y-ij} + e_{2-z} \cdot V_{z-ij} \\ V_{\text{axial-3}-ij} &= \frac{\lambda(\Delta\Phi_{3-ij} - \Phi_{\text{shift}-3})}{4\pi\tau n} \\ &= e_{3-x} \cdot V_{x-ij} + e_{3-y} \cdot V_{y-ij} + e_{3-z} \cdot V_{z-ij}. \quad (5) \end{aligned}$$

By using the known beam geometry (vectors $\vec{e}_1, \vec{e}_2, \vec{e}_3$), we can now solve the system of equations [Eq. (5)] for each pixel position ij with its individual set of axial velocities, $V_{\text{axial-}k-ij}$. This leads to the distribution of the three velocity components, V_{x-ij}, V_{y-ij}, V_{z-ij} of the flowing particles. The total flow can then be obtained by integrating the velocity values over the scanned area of interest. The postprocessing algorithm is outlined in a flow chart in Fig. 4.

For postprocessing, a PC featuring an Intel i7 CPU (3.2 GHz) with 24 GB RAM was used running a 64 bit Windows 7 operating system. Postprocessing of a typical data set, consisting of 50 B-scans (1024 A-scans each), with a nonoptimized Labview program took approximately 5 min.

3 Results

To demonstrate the performance of our three-beam DOCT system *in vitro*, we performed measurements on a rotating disc and a flow phantom. In a next step, we conducted *in-vivo* measurements on human retinal blood vessels.

3.1 *In-Vitro Measurements*

3.1.1 *Rotating disk*

In order to prove the functionality of our setup and to calibrate the instrument in a simple and well defined experiment, measurements on a rotating and tiltable disc were performed (cf. Fig. 5). The stationary movement of the disc made it possible to avoid scanning.

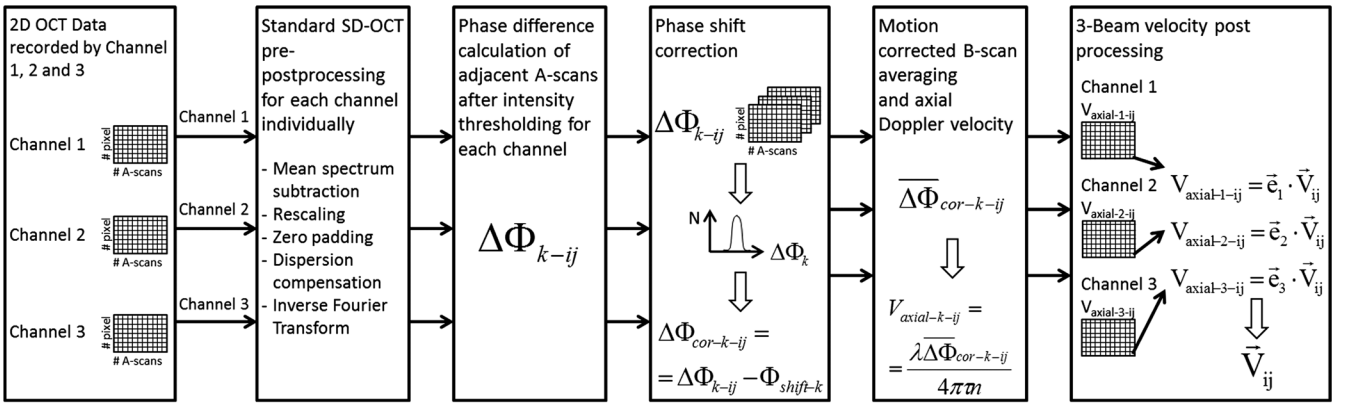

Fig. 4 Flow chart of the algorithm used for postprocessing of the three-beam DOCT measurements.

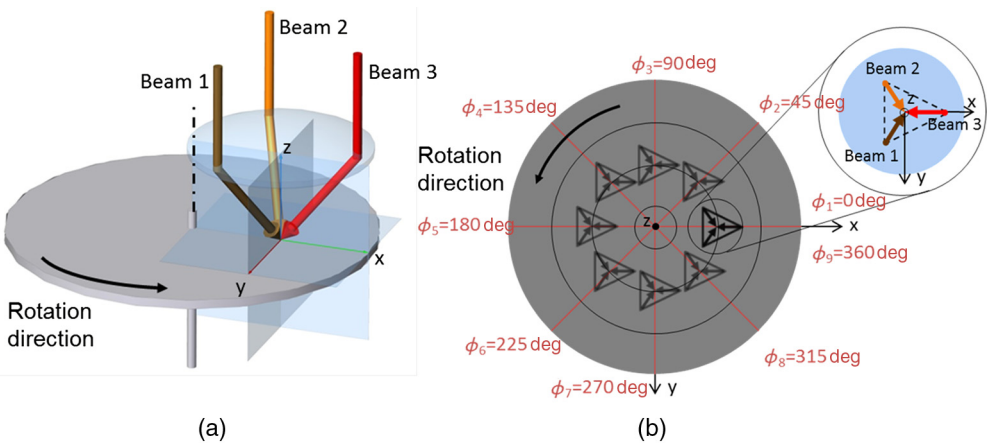

Fig. 5 Sketch of the measurement geometry and sampling points for rotating disc measurements in the *XY*-plane. (a) 3-D model of beam and sample alignment and (b) sketch of the measurement points.

For the computation of the velocity vector components, knowledge of the exact beam geometry plays a crucial role in our approach. We used the following calibration procedure to ensure correct beam geometry: The galvo scanners were set at a fixed position and a constant angular velocity was set for the disc. By choosing a measurement spot at a certain radius, the velocity vector was defined. Knowledge of the velocity vector provides the expected phase differences $\Delta\Phi$ for the respective measurement directions (channels) during that measurement. In a next step, the focusing lens was aligned orthogonal to the optical axis while the $\Delta\Phi$ values were monitored. After the expected phase differences for all three measurement directions were achieved, the optical axis and the equilateral triangular pyramid height were assumed to be collinear and the measurement geometry was regarded as correct.

After the alignment procedure, measurements were performed for various settings. At each setting, 1024 A-scans were recorded and phase differences were averaged in the complex space. The averaged values of $\Delta\Phi$ were used to calculate the three axial velocity components $V_{\text{axial-1,2,3}}$ corresponding to the three measurement directions [Eq. (1)], and with equation system (3) the velocity components V_x, V_y, V_z were obtained.

For the first test, the disc was aligned orthogonal to the optical axis (i.e., parallel to the $x-y$ plane) and the angular velocity was kept constant. At a distance of 9 mm from the disc center, points separated by 45 deg were measured. Figure 5 shows a sketch of the alignment of beams and rotating disc as well as an overview regarding the measurement points.

Figure 6 shows the results. Velocity components V_x, V_y, V_z and the absolute velocity are shown as a function of sampling point position along a circle with the radius = 9 mm. The preset absolute velocity for this angular velocity and radius was 20.0 mm/s. This is in good agreement with the measured

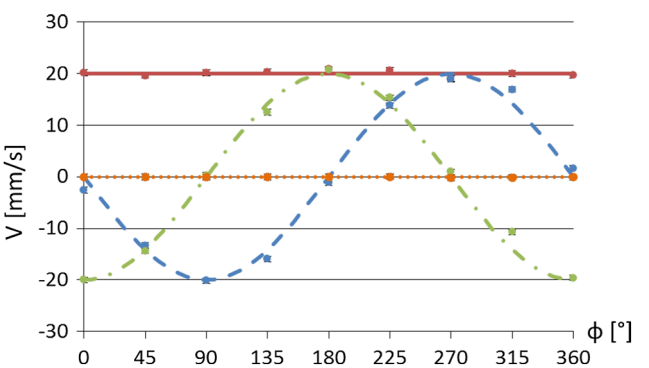

Fig. 6 Graph of velocity components measured for the disk rotating in the *XY*-plane: solid red line: expected absolute velocity; red dots: measured absolute velocity; dashed blue line: expected V_x; blue dots: measured V_x; dash-dotted green line: expected V_y; green dots: measured V_y; dotted orange line: expected V_z; orange dots: measured V_z; error bars represent the standard deviation of the absolute velocity.

absolute velocity of 20.2 ± 0.6 mm/s (mean $\pm$ standard deviation). As expected, V_x and V_y oscillate in a sinusoidal manner along the circle circumference and are 90 deg out-of-phase while V_z is close to zero. For estimating the error of x, y, and z velocity components (error bars in Fig. 6), we took the standard deviation for the absolute velocity (0.6 mm/s) as the highest expected error for the respective components.

In order to demonstrate the performance of our method to measure the z velocity component, we conducted a further test where the disc was tilted between $\rho = 0$ deg and $\rho = 18$ deg around the x-axis in steps of 2 deg. Measurements were taken at a distance of 3 mm to the center of the disc. A schematic of the test setup and the obtained data can be seen in Fig. 7. The preset absolute velocity at the measurement position was 6.7 mm/s. The measured absolute velocity of 6.9 ± 0.1 mm/s is in good agreement. Velocity components V_x, V_y, and V_z as well as the absolute velocity are shown as a function of tilt angle ρ. As expected, V_z shows an approximately linear increase with ρ within this range of the tilt angle, while V_y slightly decreases and V_x remains close to zero (the slight increase of V_x with ρ is probably caused by slight deviations of the measured position from the x-axis). For an approximate error estimation, we used again the standard deviation of the absolute velocity.

3.1.2 *Flow phantom*

To demonstrate the capability of our method to measure flow quantitatively, we performed measurements in a flow phantom consisting of a glass capillary perfused with a scattering fluid. To illustrate the velocity vector reconstruction for all three-dimensions (3-D), the capillary was rotated in planes orthogonal and parallel to the optical axis.

Outer and inner diameters of the capillary were 1.0 and 0.3 mm, respectively. As a scattering medium, we used milk diluted with water in a ratio of 1:2. A special mount, providing three rotational degrees of freedom, was used to align the sample. In order to maintain an accurate and constant flow in the capillary during the measurement, an injection pump for medical applications was used (MGVG Combimat, adjustable flow range 0.1–190 ml/h leading to mean velocities of 0.4–750 mm/s for a capillary diameter of 0.3 mm).

Operating the system at a line scan rate of 20 kHz, we recorded 20 B-scans consisting of 1024 A-scans at a constant B-scan position. The scanned length was 1.2 mm. Scanning changes the beam geometry as the measurement beams move through the optics and the sample. These geometry alterations can lead to systematic errors in the velocity calculation. We considered these effects by calculating the beam geometry as a function of galvo scanner position. This procedure yields new beam geometry vectors $(\vec{e}_1, \vec{e}_2, \vec{e}_3)$ for each measurement spot on the sample. These vectors were then inserted into our standard postprocessing procedure. After compensating the effect in postprocessing, we compared the obtained results with the original values. No significant difference was observed for the small scan angle used (~2.5 deg). Therefore, we omitted the described beam geometry correction for small scanning angles.

For the measurements, the mutual focal plane of the three sampling beams was aligned in the center of the capillary while the zero-delay was shifted to the capillary edge. The calibration procedure was similar to the one performed for the rotating disc. For a known capillary orientation, a constant flow was set at the injection pump. Without scanning, the signal phase shift obtained from the scattering fluid along a single depth profile was monitored. The capillary orientation defined the velocity vector orientation and the focusing lens was aligned until the expected phase differences for all three channels were achieved.

In a first experiment, we demonstrate the velocity vector reconstruction within a plane orthogonal to the optical axis. Figure 8 shows a schematic of sample and beam geometry. A constant flow velocity of 5.9 mm/s (mean velocity over the whole profile) was set at the injection pump. Measurements were taken at different settings of the capillary orientation angle φ, varying between 20 deg and 160 deg. A set of images illustrating the reconstruction method for a measurement at $\varphi = 45$ deg can be seen in Fig. 9. The left-hand column [Fig. 9(a)] shows intensity B-scans obtained in the three channels. The next column [Fig. 9(b)] shows the corresponding averaged phase difference images of the capillary center. Gray pixels indicate areas where the intensity threshold was not met (essentially indicating the glass walls of the capillary). The third column [Fig. 9(c)] shows the reconstructed velocity components V_x, V_y, V_z. Because the capillary was oriented at $\varphi = 45$ deg,

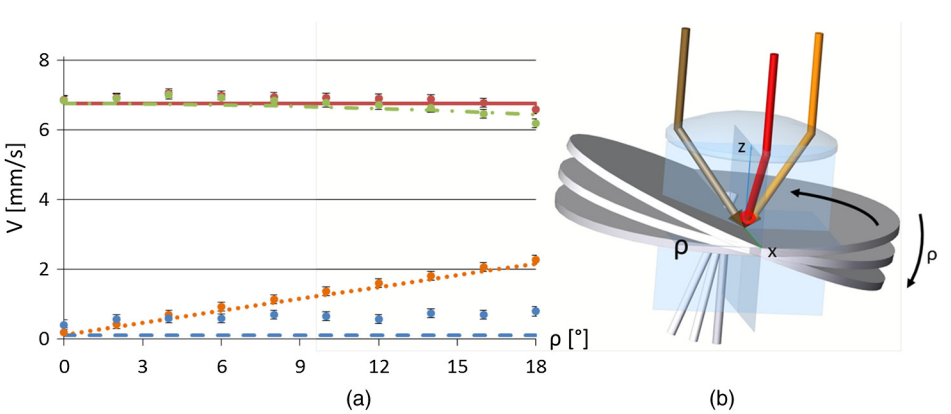

Fig. 7 Measurements in a tilted rotating disk. (a) Graph of velocity components: solid red line: expected absolute velocity; red dots: measured absolute velocity; dashed blue line: expected V_x; blue dots: measured V_x; dash-dotted green line: negative expected V_y; green dots: negative measured V_y; dotted orange line: negative expected V_z; orange dots: negative measured V_z; error bars represent the standard deviation of the absolute velocity and (b) measurement geometry.

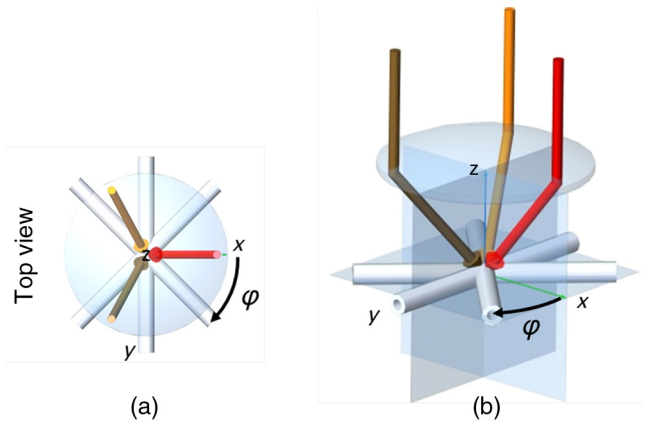

Fig. 8 Sketch of the measurement geometry for *in-vitro* capillary measurements in the *XY*-plane. (a) Top view and (b) 3-D model.

the components V_x and V_y are equal, while $V_z = 0$ (since the capillary is in the *XY*-plane), as expected. Figure 9(d) shows a 3-D plot of the absolute velocity $|V|$, showing the expected parabolic velocity profile.

Figure 10 shows a plot of (mean) velocity components V_x (blue), V_y (green), V_z (orange) and of the absolute velocity (red) as a function of angle φ. The expected values are indicated by lines, the measured values by circle symbols. The error bars equal the standard deviation of the absolute velocity, calculated over the data obtained at the different settings of φ. As can be seen, there is some discrepancy between expected and measured values (on average 15% for the absolute velocity). One reason for this discrepancy might be the refraction of the sampling beams at the glass capillary which causes a local deviation from the expected beam geometry.

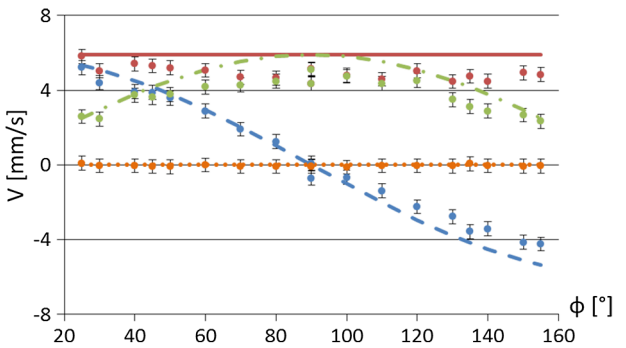

Fig. 10 Graph of mean velocities as measured in the *XY*-plane at angles between $\varphi = 20$ deg and $\varphi = 160$ deg. Solid red line: expected mean absolute velocity; red circle symbols: measured mean absolute velocity; dashed blue line: expected mean V_x; blue circles: measured mean V_x; dash-dotted green line: expected mean V_y; green circles: measured mean V_y; dotted orange line: expected mean V_z; orange circles: measured mean V_z; error bars: standard deviation of the absolute velocity.

In a second experiment, we demonstrate the velocity vector reconstruction within a plane parallel to the optical axis (*YZ*-plane). The orientation angle ρ was varied between 0 deg and 30 deg. The flow within the capillary was set to 1.9 mm/s. A sketch of the beam and sample geometry can be seen in Fig. 11.

Figure 12 shows the results for a capillary orientation of $\rho = 20$ deg. All three phase difference tomograms, $\Delta\Phi_{1-3}$, show a large phase shift [Fig. 12(b)]. This can be explained by the fact that the velocity components along the directions of the three sampling beams are now considerably larger than for the case of the capillary within the *XY*-plane. As expected, the reconstructed velocity component V_x is close to zero, while V_y and V_z have nonzero values [Fig. 12(c)]. A nearly parabolic

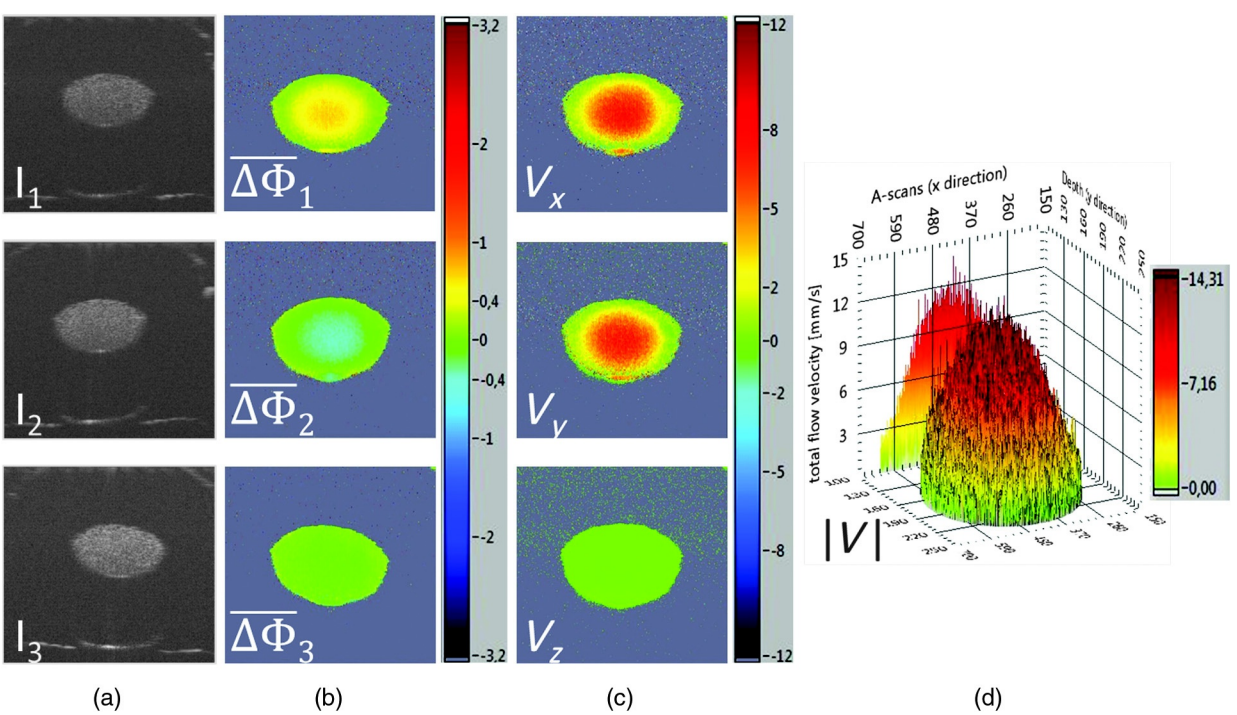

Fig. 9 DOCT images obtained for a capillary measurement at $\varphi = 45$ deg in the *XY*-plane. (a) Intensity images of the three channels; (b) averaged phase difference images of the capillary center (rad); (c) velocity components (mm/s); and (d) 3-D plot of absolute velocity $|V|$ over the capillary core (mm/s).

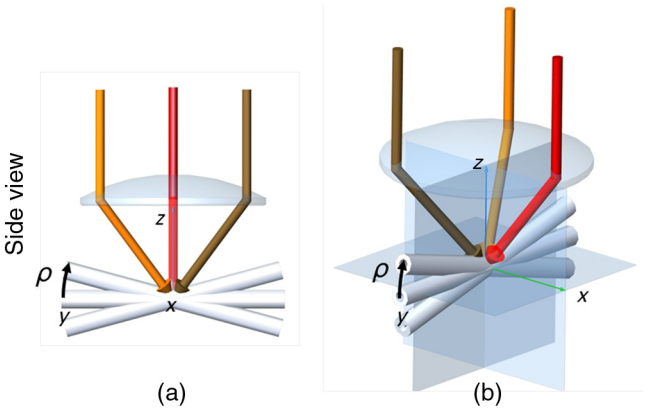

Fig. 11 Sketch of the measurement geometry for *in-vitro* capillary measurements in the *YZ*-plane. (a) Side-view and (b) 3-D model.

velocity profile of the absolute velocity is again visible [Fig. 12(d)].

Figure 13 shows a plot of velocity component V_x (blue), V_y (green), V_z (orange) and of the absolute velocity (red) as a function of tilt angle ρ. Lines show expected values, circle symbols measured values; the error bars equal the standard deviation obtained for the measured absolute velocity values across all settings of ρ. In comparison to the preset absolute velocity of 1.9 mm/s, the measured value of 1.7 ± 0.2 mm/s shows a good agreement. Deviations between expected and measured values are again likely caused by a distortion of the beam geometry by refraction at the glass capillary.

3.2 *In-Vivo Measurements*

To demonstrate the functionality of our setup for *in vivo* retinal imaging, measurements were performed in the eye of a healthy volunteer after full informed consent was obtained. The axial

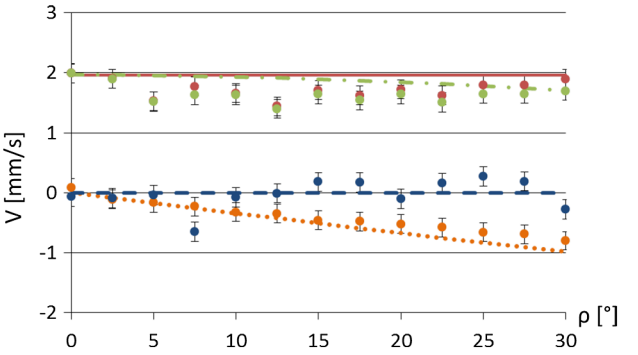

Fig. 13 Graph of mean velocities as measured in *YZ* plane at angles between $\rho = 0$ deg and $\rho = 30$ deg. Solid red line: expected mean absolute velocity; red circle symbols: measured mean absolute velocity; dashed blue line: expected mean V_x; blue circles: measured mean V_x; dash-dotted green line: expected mean V_y; green circles: measured mean V_y; dotted orange line: expected mean V_z; orange circles: measured mean V_z; error bars: standard deviation of the absolute velocity.

eye length was measured by partial coherence interferometry[48] (Zeiss IOL Master) to calculate the exact beam geometry for the flow measurement. To ensure the correct beam geometry, the focal plane position was adjusted by shifting the second lens of the second telescope T_2 (cf. Fig. 2) along the optical axis. A correct setting of the mutual focal plane of the three beams was achieved when the volunteer confirmed the fusion of three scanning lines to a single line. Furthermore, an online preview was used in order to ensure that the respective blood vessels were in the same position for all three measurement channels.

Imaging was done at an A-line frequency of 20 kHz. The scanning distance was approximately 1 mm or 3 deg. For one measurement, we recorded 50 B-scans at the same position comprising 1024 A-scans each. The subject heart beat rate was

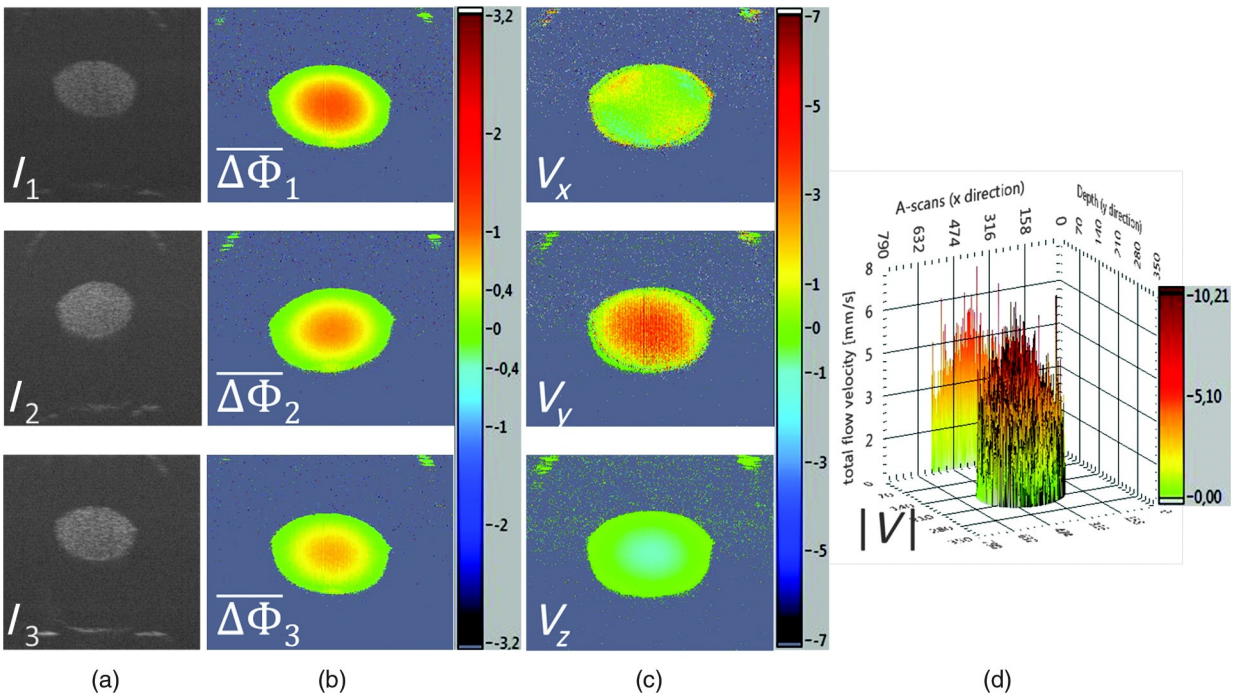

(a) (b) (c) (d)

Fig. 12 DOCT images obtained for a capillary measurement at $\rho = 20$ deg in the *YZ* plane. (a) Intensity images; (b) averaged phase difference images of the capillary center (rad); (c) velocity components (mm/s); (d) 3-D plot of the absolute velocity $|V|$ over the capillary core (mm/s).

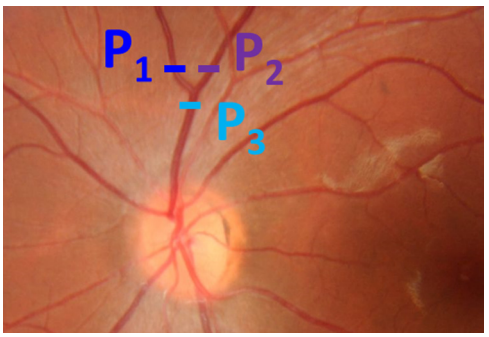

Fig. 14 Fundus photo of the left eye of a healthy human volunteer. P_1, P_2, P_3: scan locations to determine the total in- and outflow at a venous bifurcation.

determined to be 70 beats/min during the measurement, and in the postprocessing an artifact free set of 15 consecutive B-scans, covering the time of one heart beat cycle, was chosen for further evaluation. Before averaging, B-scans were aligned to correct for eye motions.

Figure 14 shows a fundus image of the measured eye. The aim was to quantify the total in- and outflow at the indicated venous bifurcation. For that purpose, measurements were performed at positions P_1, P_2, and P_3. A typical set of tomograms obtained by the measurement at the venous inflow position P_2 can be seen in Fig. 15. The second column [Fig. 15(b)] shows averaged phase difference images of 15 B-scans. The vessel can be easily distinguished from the static tissue in all three channels. The velocity component images [Fig. 15(c)] show larger

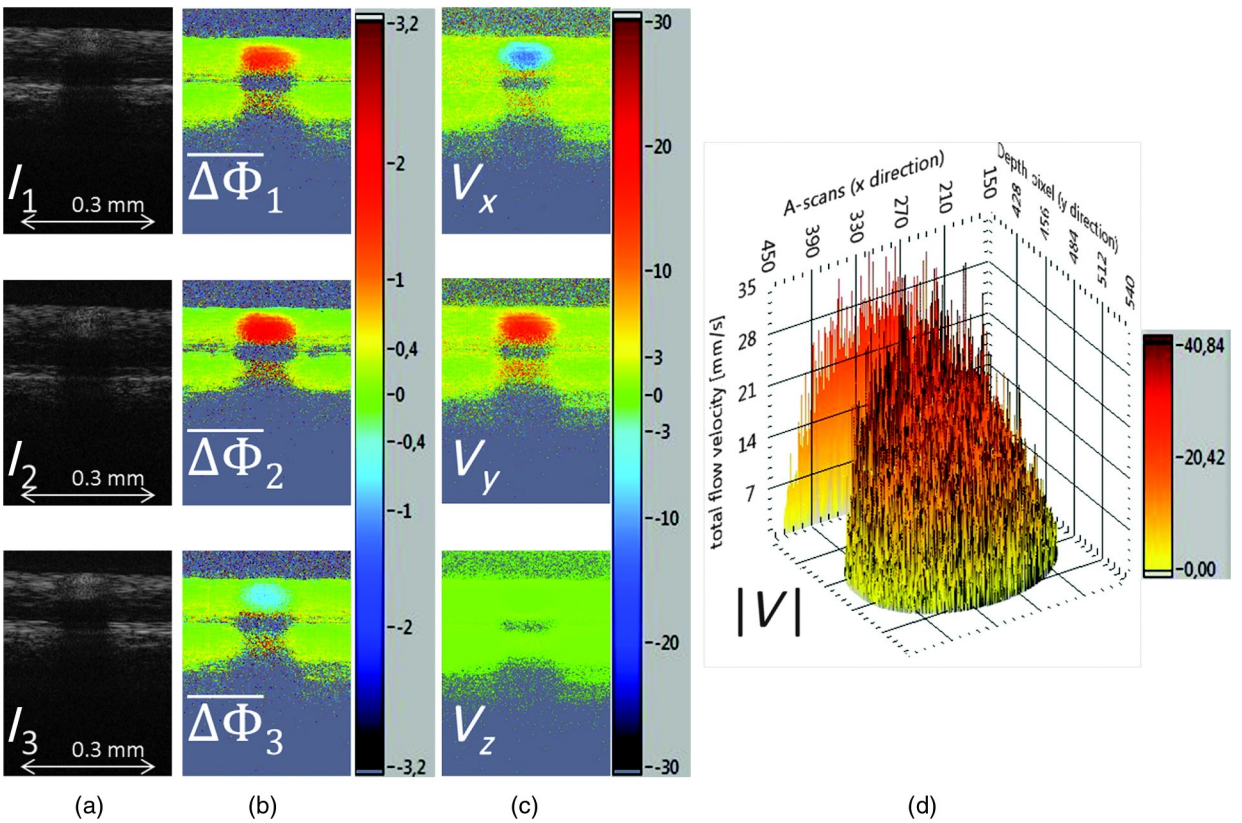

Fig. 15 DOCT images obtained from a retinal vessel (location P_2 in Fig. 14) in a healthy human eye. (a) Intensity images; (b) phase difference images of 15 averaged B-scans (rad); (c) velocity components (mm/s); (d) 3-D plot of the absolute velocity distribution over the blood vessel cross section (mm/s).

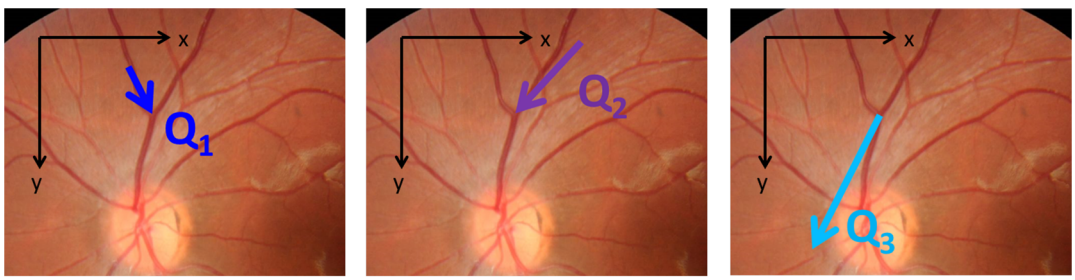

Fig. 16 Reconstructed blood flow in indicated branches of venous bifurcation. Arrows orientation and length indicate the blood flow direction and rate (in μl/s), respectively.

Table 1 Summary of blood flow measurement results on a human retinal venous bifurcation.

	Inflow Q_1	Inflow Q_2	Outflow Q_3
Ø (mm)	0.12	0.14	0.17
V_x (mm/s)	4.5	−9.8	−6.1
V_y (mm/s)	8.7	10.1	12.0
V_z (mm/s)	−0.8	−0.5	−1.3
$\|V\|$ (mm/s)	9.8	13.7	13.5
Q (μl/s)	0.12	0.22	0.31

velocities only for components V_x and V_y, while V_z is close to zero, as expected for a vessel away from the optic nerve head. V_x and V_y were averaged over the vessel cross section and the velocity vector in the XY-plane was determined. The vector angle of 135 deg to the x-direction at P_2 is in good agreement with the vessel orientation at this point in the fundus photo. Flow rates Q_1, Q_2, Q_3 at P_1, P_2, and P_3 were calculated by integrating the velocity components over the vessel areas.

Figure 16 illustrates flow orientation and quantity for the three vessel branches of the bifurcation obtained at the three measurement locations. The length of the respective arrow is proportional to the flow quantity (in μl/s); the arrow orientation corresponds to the retrieved flow vector orientation. The vessel diameters were measured to be between 0.12 and 0.17 mm while the total flow rate in the respective vessels showed a range of 0.11–0.31 μl/s.

These results are in good agreement with the results found in the literature: measurements done with laser Doppler velocimetry (LDV)[49] suggest total flow rates of 0.10–0.25 μl/s for the same vessel diameter range. A more recently published paper[24] using a Fourier domain D-OCT system reported flow rates of 0.05–0.23 μl/s for vessel diameters of 0.070–0.152 mm.

Table 1 summarizes the results. The total measured inflow (0.34 μl/s) is in good agreement with the total measured outflow (0.31 μl/s).

4 Discussion and Conclusion

We developed a new three-beam DOCT system that allows the 3-D reconstruction of flow orientation and the determination of the absolute flow velocity, without the need for information on the orientation of the vessel. We demonstrated the functionality of the new system in a simple test object, a glass capillary, and—to the best of our knowledge for the first time—in the retina of a human volunteer *in vivo*.

By measurements performed on a rotating disc, we demonstrated the functionality of our system for velocity vector reconstruction in all 3-D. Scanning a single point on an evenly moving object, a good correlation between preset velocities and measured velocities was observed. It should be mentioned that with this simple test object, no scanning was performed. In the more realistic flow phantom, we tested the performance of our system in a real imaging situation, i.e., with beam scanning in operation. By pumping a scattering fluid through the capillary, a constant flow was provided for measurements. Aligning the flow in a plane orthogonal and parallel to the optical axis, we showed that our approach allows one to reconstruct the velocity vector in all 3-D for arbitrary velocity orientations. The observed deviations between expected and measured flow values are probably caused by refractions at the glass capillary which distort the sampling beam geometry. Since the refractive index differences between vessel walls and surrounding tissue are considerably smaller than those between the capillary glass and its adjacent media (air and aqueous solution) we expect that this effect will be lower for measurements in tissue. However, since the local distribution of refractive index in tissue is not exactly known, this effect might cause minor deviations of velocity measurements from true values.

Applying the new three-beam DOCT technique to the human eye yielded retinal blood velocity and blood flow results which are in the same range as those measured by other methods.[24,35,49,50] Furthermore, the good agreement between bifurcation in- and outflow is very promising and supports the reliability of the measurements. Present shortcomings comprise the rather low transversal resolution of ~60 μm, caused by the low numerical aperture of the beams used, and the presently complicated alignment procedure for *in-vivo* measurements that requires feedback from the subject. The former problem might be mitigated by using collimators with a larger beam diameter (although there is a trade-off with beam separation), and the latter problem might be solved by adding a fundus view capable of resolving the laser beams on the retina for quick and objective focusing.

To summarize, we developed a new three-beam SD-DOCT system and demonstrated its ability to reconstruct the velocity vector in 3-D. The instrument was demonstrated in test samples and in the retina of a human volunteer *in vivo*. Reliable quantification of the flow was demonstrated by measuring in- and outflow at a venous bifurcation.

Acknowledgments

Financial support from the European Union (project FUN OCT, FP7 HEALTH, Contract No. 201880) and from the Austrian Science Fund (FWF Grant No. P19624-B02) is gratefully acknowledged.

References

1. D. Huang et al., "Optical coherence tomography," *Science* **254**(5035), 1178–1181 (1991).
2. A. F. Fercher et al., "Optical coherence tomography—principles and applications," *Rep. Prog. Phys.* **66**(2), 239–303 (2003).
3. W. Drexler and J. G. Fujimoto, *Optical Coherence Tomography: Technology and Applications*, Springer, Berlin (2008).
4. W. Drexler and J. G. Fujimoto, "State-of-the-art retinal optical coherence tomography," *Prog. Retinal Eye Res.* **27**(1), 45–88 (2008).
5. W. Geitzenauer, C. K. Hitzenberger, and U. M. Schmidt-Erfurth, "Retinal optical coherence tomography: past, present and future perspectives," *Br. J. Ophthalmol.* **95**(2), 171–177 (2011).
6. X. J. Wang, T. E. Milner, and J. S. Nelson, "Characterization of fluid-flow velocity by optical Doppler tomography," *Opt. Lett.* **20**(11), 1337–1339 (1995).
7. Z. Chen et al., "Optical Doppler tomographic imaging of fluid flow velocity in highly scattering media," *Opt. Lett.* **22**(1), 64–66 (1997).
8. J. A. Izatt et al., "*In vivo* bidirectional color Doppler flow imaging of picoliter blood volumes using optical coherence tomograghy," *Opt. Lett.* **22**(18), 1439–1441 (1997).
9. Z. Chen et al., "Optical Doppler tomography," *IEEE J. Sel. Top. Quant. Electron.* **5**(4), 1134–1142 (1999).
10. Y. H. Zhao et al., "Phase-resolved optical coherence tomography and optical Doppler tomography for imaging blood flow in human skin

with fast scanning speed and high velocity sensitivity," *Opt. Lett.* **25**(2), 114–116 (2000).
11. R. A. Leitgeb et al., "Real-time assessment of retinal blood flow with ultrafast acquisition by color Doppler Fourier domain optical coherence tomography," *Opt. Express* **11**(23), 3116–3121 (2003).
12. B. R. White et al., "*In vivo* dynamic human retinal blood flow imaging using ultra-high-speed spectral domain optical Doppler tomography," *Opt. Express* **11**(25), 3490–3497 (2003).
13. S. Makita et al., "Optical coherence angiography," *Opt. Express* **14**(17), 7821–7840 (2006).
14. A. H. Bachmann et al., "Resonant Doppler flow imaging and optical vivisection of retinal blood vessels," *Opt. Express* **15**(2), 408–422 (2007).
15. A. Szkulmowska et al., "Three-dimensional quantitative imaging of retinal and choroidal blood flow velocity using joint spectral and time domain optical coherence tomography," *Opt. Express* **17**(13), 10584–10598 (2009).
16. M. Szkulmowski et al., "Flow velocity estimation using joint spectral and time domain optical coherence tomography," *Opt. Express* **16**(9), 6008–6025 (2008).
17. R. K. Wang et al., "Three dimensional optical angiography," *Opt. Express* **15**(7), 4083–4097 (2007).
18. L. An et al., "High-resolution wide-field imaging of retinal and choroidal blood perfusion with optical microangiography," *J. Biomed. Opt.* **15**(2), 026011 (2010).
19. Y. K. Tao, A. M. Davis, and J. A. Izatt, "Single-pass volumetric bidirectional blood flow imaging spectral domain optical coherence tomography using a modified Hilbert transform," *Opt. Express* **16**(16), 12350–12361 (2008).
20. J. Barton and S. Stromski, "Flow measurement without phase information in optical coherence tomography images," *Opt. Express* **13**(14), 5234–5239 (2005).
21. Y. Wang and R. Wang, "Autocorrelation optical coherence tomography for mapping transverse particle-flow velocity," *Opt. Lett.* **35**(21), 3538–3540 (2010).
22. H. Asai, "Proposal of a simple method of fluorescence correlation spectroscopy for measuring the direction and magnitude of a flow of fluorophores," *Jpn. J. Appl. Phys.* **19**(11), 2279–2282 (1980).
23. J. Lee et al., "Dynamic light scattering optical coherence tomography," *Opt. Express* **20**(20), 22262–22277 (2012).
24. Y. Wang et al., "Retinal blood flow measurement by circumpapillary Fourier domain Doppler optical coherence tomography," *J. Biomed. Opt.* **13**(6), 064003 (2008).
25. A. S. G. Singh et al., "Stable absolute flow estimation with Doppler OCT based on virtual circumpapillary scans," *Biomed. Opt. Express* **1**(4), 1047–1059 (2010).
26. S. Zotter et al., "Visualization of microvasculature by dual-beam phase-resolved Doppler optical coherence tomography," *Opt. Express* **19**(2), 1217–1227 (2011).
27. S. Makita et al., "Comprehensive *in vivo* micro-vascular imaging of the human eye by dual-beam-scan Doppler optical coherence angiography," *Opt. Express* **19**(2), 1271–1283 (2011).
28. F. Jaillon et al., "Enhanced imaging of choroidal vasculature by high-penetration and dual-velocity optical coherence angiography," *Biomed. Opt. Express* **2**(5), 1147–1158 (2011).
29. S. M. Daly, C. Silien, and M. J. Leahy, "Feasibility of capillary velocity assessment by statistical means using dual-beam spectral-domain optical coherence tomography: a preliminary study," *J. Biophoton.* **6**(9), 718–732 (2013).
30. D. P. Dave and T. E. Milner, "Doppler-angle measurement in highly scattering media," *Opt. Lett.* **25**(20), 1523–1525 (2000).
31. A. Royset et al., "Quantitative measurements of flow velocity and direction using transversal Doppler optical coherence tomography," *Proc. SPIE* **6079**, 607925 (2006).
32. C. J. Pedersen et al., "Measurement of absolute flow velocity vector using dual-angle, delay-encoded Doppler optical coherence tomography," *Opt. Lett.* **32**(5), 506–508 (2007).
33. Y. C. Ahn, W. Jung, and Z. Chen, "Quantification of a three-dimensional velocity vector using spectral-domain Doppler optical coherence tomography," *Opt. Lett.* **32**(11), 1587–1589 (2007).
34. R. M. Werkmeister et al., "Bidirectional Doppler Fourier-domain optical coherence tomography for measurement of absolute flow velocities in human retinal vessels," *Opt. Lett.* **33**(24), 2967–2969 (2008).
35. R. M. Werkmeister et al., "Measurement of absolute blood flow velocity and blood flow in the human retina by dual-beam bidirectional Doppler Fourier-domain optical coherence tomography," *Invest. Ophthalmol. Visual Sci.* **53**(10), 6062–6071 (2012).
36. C. Blatter et al., "Dove prism based rotating dual beam bidirectional Doppler OCT," *Biomed. Opt. Express* **4**(7), 1188–1203 (2013).
37. G. Magyar and L. Mandel, "Interference fringes produced by superposition of two independent maser light beams," *Nature* **198**(487), 255–256 (1963).
38. A. F. Fercher et al., "Measurement of intraocular distances by backscattering spectral interferometry," *Opt. Commun.* **117**(1–2), 43–48 (1995).
39. G. Haeusler and M. W. Lindner, "Coherence Radar" and "Spectral Radar"—new tools for dermatological diagnosis," *J. Biomed. Opt.* **3**(1), 21–31 (1998).
40. M. Wojtkowski et al., "*In vivo* human retinal imaging by Fourier domain optical coherence tomography," *J. Biomed. Opt.* **7**(3), 457–463 (2002).
41. A. G. Podoleanu, G. M. Dobre, and D. A. Jackson, "En-face coherence imaging using galvanometer scanner modulation," *Opt. Lett.* **23**(3), 147–149 (1998).
42. B. Baumann et al., "Single camera based spectral domain polarization sensitive optical coherence tomography," *Opt. Express* **15**(3), 1054–1063 (2007).
43. S. Zotter et al., "Large-field high-speed polarization sensitive spectral domain OCT and its applications in ophthalmology," *Biomed. Opt. Express* **3**(11), 2720–2732 (2012).
44. N. Suehira et al., "Three-beam spectral-domain optical coherence tomography for retinal imaging," *J. Biomed. Opt.* **17**(10), 106001 (2012).
45. "American National Standards for safe use of lasers," in *ANSI Z 136.1*, A. N. S. Institute, Ed., Laser Institute of America, Orlando (2000).
46. , "Safety of laser products—part 1: equipment classification and requirements," in *IEC 60825-1 Ed. 2*, I. E. Commission, Ed., International Electrotechnical Commission, Geneva (2001).
47. A. Szkulmowska et al., "Phase-resolved Doppler optical coherence tomography limitations and improvements," *Opt. Lett.* **33**(13), 1425–1427 (2008).
48. C. K. Hitzenberger, "Optical measurement of the axial eye length by laser Doppler interferometry," *Invest. Ophthalmol. Visual Sci.* **32**(3), 616–624 (1991).
49. C. E. Riva et al., "Blood velocity and volumetric flow-rate in human retinal vessels," *Invest. Ophthalmol. Visual Sci.* **26**(8), 1124–1132 (1985).
50. B. Baumann et al., "Total retinal blood flow measurement with ultrahigh speed swept source/Fourier domain OCT," *Biomed. Opt. Express* **2**(6), 1539–1552 (2011).